European Journal of Nuclear Medicine and Molecular Imaging (2019) 46:2099–2111
https://doi.org/10.1007/s00259-019-04419-z

ORIGINAL ARTICLE

Evaluation of pharmacokinetic modeling strategies for in-vivo quantification of tau with the radiotracer [^{18}F]MK6240 in human subjects

Nicolas J. Guehl[1] · Dustin W. Wooten[1] · Daniel L. Yokell[1] · Sung-Hyun Moon[1] · Maeva Dhaynaut[1] · Samantha Katz[1] · Kirsten A. Moody[1] · Codi Gharagouzloo[1] · Aurélie Kas[2] · Keith A. Johnson[1] · Georges El Fakhri[1] · Marc D. Normandin[1]

Received: 3 January 2019 / Accepted: 18 June 2019 / Published online: 22 July 2019

Abstract

Purpose [^{18}F]MK6240 was developed for PET imaging of tau aggregates, which are implicated in Alzheimer's disease. The goal of this work was to evaluate the kinetics of [^{18}F]MK6240 and to investigate different strategies for in-vivo quantification of tau aggregates in humans.

Methods Thirty-five subjects, consisting of 18 healthy controls (CTRL), 11 subjects with mild cognitive impairment (MCI) and six with Alzheimer's Disease (AD), underwent dynamic [^{18}F]MK6240 PET scans. Arterial blood measurements were collected in 16 subjects (eight CTRLs, six MCIs and two AD) to measure whole blood and plasma concentration time courses. Radiometabolite analysis was performed on a subset of plasma samples. Various compartmental model configurations as well as the Logan and multilinear analysis (MA1) graphical methods with arterial plasma input function were tested. Simplified reference tissue methods were investigated, including Logan distribution volume ratio (DVR), multilinear reference tissue method (MRTM2), and static SUV ratio using the cerebellum as a reference region.

Results Whole blood:plasma ratio stabilized to 0.66 ± 0.01 after 15 min. Percent parent in plasma (%PP) followed a single exponential and ranged from 0 to 10% at 90 min. [^{18}F]MK6240 in gray matter peaked quickly (SUV > 2 at ~3 min). The preferred compartmental model was a reversible two-tissue compartment model, with the blood contribution included as a model parameter (2T4k1v). Compartmental and graphical analysis methods with arterial input functions yielded concordant results, but rapid metabolism raised challenges for blood-based quantification. MCI and AD subjects demonstrated a broad range of V_T as compared to CTRL subjects. DVR from MRTM2 and Logan reference tissue methods correlated with DVR calculated indirectly from compartmental modeling, but underestimation was observed in data sets with very high binding (DVR > 3). SUVR also underestimated indirect DVR from blood-based analyses in high binding regions, although a non-linear relationship was exhibited.

Conclusions [^{18}F]MK6240 exhibited a wide dynamic range of uptake, with binding patterns in MCI/AD subjects consistent with neurofibrillary tau deposition patterns. Linearized reference tissue methods using an estimated average tissue-to-plasma efflux constant $\overline{k'_2}$ and static SUVR agreed well with blood-based methods for most data sets; however, discrepancies were noted in the highest binding cases. Caution should therefore be exercised in application of simplified methods to such data sets, and in quantitative interpretation of corresponding outcomes.

Keywords Positron emission tomography · [^{18}F]MK6240 · Tau · Pharmacokinetics · Kinetic modeling

Nicolas J. Guehl and Dustin W. Wooten contributed equally to this work.

This article is part of the Topical Collection on Neurology

Electronic supplementary material The online version of this article (https://doi.org/10.1007/s00259-019-04419-z) contains supplementary material, which is available to authorized users.

✉ Nicolas J. Guehl
nguehl@pet.mgh.harvard.edu

[1] Gordon Center for Medical Imaging, Department of Radiology, Massachusetts General Hospital, Harvard Medical School, Boston, MA, USA

[2] AP-HP, Department of Nuclear Medicine, Pitié-Salpêtrière Hospital, Sorbonne University, UPMC Paris 06, CNRS UMR 7371, INSERM U1146, 75013 Paris, France

Introduction

Alzheimer's disease (AD) represents the most common form of dementia, accounting for 60 to 80% of dementia cases in

the world. Two key hallmarks of this disease are the abnormal accumulation of hyper-phosphorylated tau proteins and amyloid beta plaques in the brain. It has been shown that the spreading of tau neurofibrillary tangles (NFT) in the brain follows a well-defined and predictable pattern [1] as the disease progresses and, unlike amyloid beta plaques, correlates with the cognitive decline associated with the disease [2, 3]. Tau pathology also plays an important role in non-AD neurodegenerative disease such as progressive supranuclear palsy cases (PSP), chronic traumatic encephalopathy (CTE), or frontotemporal dementia (FTD). Much effort has recently been put into the development of PET radiotracers for in-vivo quantification of tau protein. However, even though the first generation of tau radiotracers has provided new insights into the progression of AD, they all present some limitations with respect to off-target and/or non-specific binding, which may limit their clinical utility [4–6]. Recently, Merck reported the discovery of [^{18}F]MK6240, a novel imaging compound for detecting tau pathology [7]. Preliminary in-vitro studies in tissues from AD and non-AD human brain donors seemed to indicate high affinity and unprecedented selectivity for binding NFT, and the first in-vivo studies in non-human primates have indicated favorable pharmacokinetics for PET imaging [8]. More recently, Betthauser et al. provided a thorough investigation of [^{18}F]MK6240 in-vivo kinetics and modeling strategies in humans, using reference tissue methods [9]. The main limitation of their work, however, was the lack of arterial blood sampling data for [^{18}F]MK6240 binding quantification, which is generally considered the gold standard for quantification of physiological processes in PET imaging. Following this work, Lolith et al. as well as Pascoal et al. presented the first in-human kinetic evaluations with arterial blood sampling, each in a subset of six subjects [10, 11]. While their results support the use of simplified semi-quantitative methods such as SUVR as a valid surrogate for NFT quantification with [^{18}F]MK6240, Lolith et al. concluded that more studies with arterial blood sampling and kinetic modeling were needed to better understand the limitations and potential bias of such outcome.

The aim of the present work was to extend previous in-human investigations for the determination of optimal modeling strategies for in-vivo quantification of tau with [^{18}F]MK6240. This includes a characterization of modeling methods using compartment modeling and arterial blood sampling as the reference, as well as the assessment of graphical and simplified methods.

Methods

Participants

As shown in Table 1, a total of 35 subjects, consisting of 18 healthy controls (CTRL), 11 subjects with mild cognitive impairment (MCI), and six subjects with Alzheimer's disease (AD), were included in this work. All subjects were identified by physicians at Massachusetts General Hospital (MGH) and underwent at least one comprehensive medical and neurological evaluation using tests such as the Mini-Mental State Examination (MMSE) and/or the Clinical Dementia Rating (CDR) scale. These subjects also underwent ^{11}C-PiB PET scans in a separate study where PiB scores were expressed as the distribution volume ratio (DVR). DVRs were calculated in a large cortical ROI that included frontal, lateral temporal, and retrosplenial cortices (FLR) using the Logan graphical method, with cerebellar gray as reference tissue, as described in Johnson et al. [12]. All subjects signed an informed consent form, and the study was approved by the institutional review board at MGH.

Data acquisition

All enrolled subjects underwent separate PET and magnetic resonance imaging (MRI) procedures.

MR imaging: Structural MRI was performed for anatomical reference. A 3-dimensional structural T1-weighted magnetization-prepared rapid gradient-echo (MPRAGE) was acquired using a 3 T Tim Trio (Siemens Medical Systems). The MPRAGE acquisitions parameters were as follows: repetition time = 2300 ms; echo time = 2.95 ms; inversion time = 900 ms; flip angle = 9°; voxel size = 1.05 × 1.05 × 1.2 mm^3 and matrix size = 256 × 240.

PET imaging: [^{18}F]MK6240 was synthesized as described in Collier et al. [13]. Eighteen participants (S1-S18) were scanned on an ECAT EXACT HR+ (CTI/Siemens). The full width at half maximum (FWHM) spatial resolutions measured at the center of the axial field of view (radial position = 1 cm) were reported to be 4.5 mm and 5.1 mm in transverse and axial direction respectively [14, 15]. Dynamic data was measured for 135 min following bolus injection of [^{18}F]MK6240. Subjects were allowed to take a 15 min break either at 60 min (S1 and S2) or at 90 min (all other subjects) post-tracer injection. Transmission scans using a ^{68}Ge rod source were acquired right before acquisition of the first PET segment as well as right after the second PET segment, for the purpose of attenuation correction. The remaining 17 subjects (S19-S35) were scanned on a Discovery MI (GE Healthcare) PET/CT scanner. The full width at half maximum (FWHM) spatial resolutions measured at the center of the axial field of view (radial position = 1 cm) were 4.3 mm and 5.1 mm in transverse and axial direction respectively. Dynamic data was measured for 120 min following bolus injection of [^{18}F]MK6240. These subjects were allowed to take a 15-min break either at 65 min (S24, S26, S29, and S34) or at 80 min (S22) post injection. Low-dose CT acquisitions were performed right before each PET segment for the purpose of attenuation correction.

Injected PET tracer activities at the time of injection were 184.5 ± 10.3 MBq (range: 153.2–200.9). Molar activity (A_m) of [^{18}F]MK6240 at the time of injection was 74.7 ± 35.9 GBq/μmol (range: 11.6–151.9). Total injected mass was 992.2 ± 848.6 ng (range: 341.5–4502.8), corresponding to 3.58 ± 3.06 nmol (range: 1.23–16.24). Arterial blood measurements were collected for 16 subjects (eight CTRLs, six MCIs and two AD), ten of which were on the ECAT EXACT HR+ (four CTRLs, five MCIs and one AD) and six of which were on the Discovery MI (four CTRLs, one MCI and one AD). A catheter was placed in the radial artery for blood sampling to permit measurement of whole blood and plasma concentrations. Arterial blood samples of up to 1 ml were collected every 30 seconds for the first 5 minutes after radiotracer injection and frequency was progressively reduced to reach 15 min at the end of the scan session. Radioactivity concentration was measured in whole-blood (WB) and subsequently in plasma following the centrifugation of WB. [^{18}F]MK6240 metabolism was measured from up to 3 ml blood samples drawn at 3, 5, 8, 15, 30, 60, 90, and up to 120 min throughout the scan. Radiometabolite analysis was performed using an automated column-switching radioHPLC system [16, 17], and eluent was fraction collected and counted on a Perkin Elmer Wizard 2480 well counter. The procedure adopted for these measurements was similar to the one described in Wooten et al. [18], except that a 62.5/37.5 sodium formate buffer/MeCN was used to backflush the catch column. Ultrafiltration measurements of plasma free fraction f_p were performed in triplicate for each subject. Briefly, plasma samples were spiked with [^{18}F]MK6240 and incubated for 15 min. Radioactive plasma solutions were added to Centrifree Ultrafiltration tubes that were centrifuged at 1500 g for 15 min at room temperature. The same procedure was repeated for a control solution (PBS) spiked with [^{18}F]MK6240 in order to correct results for binding to the ultrafiltation tube membrane, and f_p was calculated as $f_p = C_{free}/C_{total}$.

Image reconstruction and processing

PET reconstruction: Dynamic PET data acquired on the ECAT EXACT HR+ (CTI/Siemens) were reconstructed using a filtered back projection algorithm while applying corrections for attenuation, scatter, random coincidences, normalization, and deadtime. Final reconstructed images had matrix sizes of 128 ×128 ×63 and voxel sizes of 2.06 × 2.06 × 2.42 mm^3. Dynamic PET data acquired on the Discovery MI (GE Healthcare) PET/CT scanner were reconstructed using a validated fully 3D time-of-flight iterative reconstruction algorithm using five iterations and 16 subsets while applying corrections for attenuation, scatter, random coincidences, normalization, and deadtime. Final reconstructed images had matrix sizes of 256 × 256 × 89 and voxel sizes of 1.17 × 1.17 × 2.8 mm^3. For both scanners, the time bins used to frame the emission data were 6 × 10s, 8 × 15s, 6 × 30s, 8 × 60s, 8 × 120s, 18 × 300s.

Image processing: Dynamic PET images were motion corrected using the method described in Alpert et al. [19]. Briefly, motion correction was performed frame by frame through rigid body registration of adjacent frames using a least-squares algorithm with Levenberg–Marquardt optimization. All MR and PET images were registered into the standard Montreal Neurological Institute (MNI) space following the procedure described in Wooten et al. [18].The dynamic PET images of the 2nd segment were summed and coregistered to the summed images of the last 20 min of the first dynamic segment. The resulting transformation matrix was applied to the dynamic PET images (segment 2) which were decay corrected to the start of the first dynamic acquisition. The two dynamic segments were then concatenated to form a single dynamic dataset. All MR and PET images were then registered into the standard Montreal Neurological Institute (MNI) space as follows. The first 10 min of the dynamic PET images were summed and rigidly co-registered to the subject's structural MR image. The MR image itself was registered into the MNI space using a 12-parameter affine transformation followed by non-linear warping (FMRIB's Linear Image Registration Tool [FLIRT] and FMRIB's Non-Linear Image Registration Tool [FNIRT] in the FMRIB Software Library [FSL] [20]). The transformation matrices were then combined and applied inversely on MNI and Harvard–Oxford atlases (available in FSL) to warp all atlases into the native PET images for extraction of time–activity curves. The regions of interest surveyed in this work included the frontal cortex, parietal cortex, occipital cortex, temporal cortex, mesial temporal cortex, precuneus, cerebellum gray (excluding the vermis), caudate, putamen, and white matter.

Arterial blood analysis

Standardized uptake value (SUV) time–activity curves (TAC) of plasma and WB were generated for inter-subject comparison by correcting the measurements for subject body weight and injected dose as $SUV(t) = [C(t) \times BW \times 1000]/ID$, where $C(t)$ is the plasma or WB concentration curve in kBq/cc, ID is the injected dose in kBq, and BW is body weight in kg. In order to obtain the percent parent in plasma (%PP) at the measured time points, background radioactivity was subtracted from the measurements, and radioactivity eluting in the [^{18}F]MK6240 peak was divided by the total activity. %PP measurements were then fitted to a sum of exponential decaying functions to generate %PP(t). Plasma arterial input functions of [^{18}F]MK6240 were then generated by correcting plasma SUV TAC for [^{18}F]MK6240 metabolism using

%PP(t) as $C_P^{Corrected} = C_P^{total}(t) \times [\%PP(t)/100]$.

[^{18}F]MK6240 brain kinetic analysis

Compartmental modeling using arterial plasma input function: Regional TACs were analyzed with various one- (1 T) and two- (2 T) tissue compartment models. The 2 T model was assessed in its irreversible (K_1-k_3 estimated, $k_4 = 0$) and reversible (K_1-k_4 estimated) configurations. For models with reversible binding, the outcome of primary interest was the macroparameter V_T (total volume of distribution, the equilibrium ratio of tracer in tissue relative to plasma which is linearly related to tracer binding to tau). Following the consensus nomenclature for imaging of reversibly binding radioligands [21], in the 1 T model K_1 (ml/min/cc) represents the rate constant for transfer from arterial plasma to tissue and k_2 (min^{-1}) the efflux rate constant of tracer from tissue to plasma, with total volume of distribution calculated as $V_T = K_1/k_2$. In the 2 T model, total volume of distribution is calculated as $V_T = K_1/k_2(1 + k_3/k_4)$. Here, K_1 represents the rate of transfer from plasma to the non-displaceable compartment in tissue, k_2 represents efflux from the non-displaceable compartment back to plasma, k_3 (min^{-1}) represents tracer binding from the non-displaceable compartment to the specifically bound compartment, and k_4 (min^{-1}) represents tracer unbinding from the specific binding compartment back to non-displaceable compartment. Alternatively, k_2 may represent efflux from a free tissue compartment, k_3 may represent binding to a non-specific binding compartment, and k_4 may represent unbinding from non-specifically bound to free compartment; this situation is mathematically indistinguishable from the aforementioned case, where k_3 and k_4 represent specific binding and unbinding processes. All models were evaluated with the contribution of radioactivity in WB to the PET signal included as a model parameter v, and also with this vascular contribution fixed to $v = 0.05$. Distribution volume ratios were calculated indirectly as $DVR = V_T(\text{target})/V_T(\text{reference})$ using cerebellar gray matter as the reference tissue as described below.

Graphical analysis using arterial plasma input function: The Logan and multilinear analysis MA1 graphical analysis techniques [22, 23] were also applied to ROI based TAC curves, and their outcomes were compared to the V_T calculated from the micro-parameters estimated by the full compartmental modeling analysis.

Reference region methods: All reference region-based analysis was performed using the cerebellar gray matter excluding the vermis. The Logan graphical method with a reference region input function [24] and MRTM2 [25] were investigated for the estimation of the distribution volume ratio (DVR). For both methods, an average tissue-to-plasma efflux constant $\overline{k'_2}$ was used and was fixed to the average of k'_2 cerebellar values ($\overline{k'_2} = 0.0126 \pm 0.0051$ min^{-1}) calculated from the 2T4k1v microparameters across subjects scanned with arterial blood sampling (as in Equation 5 from Logan 2003 [26]). We also investigated the use of the full reference tissue model (FRTM) [27] as well as a simplified reference tissue model (SRTM) [28]. The most simplified analysis investigated in this work relied on the standard uptake value (SUV). SUV ratios (SUVR) were calculated from PET data acquired from 70 to 90 min ($SUVR_{70–90min}$) and from 90 to 120 min ($SUVR_{90–120min}$) post tracer injection. The outcomes of these reference region-based methods were compared to DVR estimates obtained from compartmental modeling with arterial plasma input function, using the full duration of the PET acquisition. $SUVR_{70–90min}$ and $SUVR_{90–120min}$ were also compared to DVR estimated with Logan and MRTM2, using the full duration of the PET acquisition. For FRTM and SRTM, DVR was calculated from the estimated binding potential BP as $DVR = BP + 1$.

Time stability of model estimates and t of graphical methods*: Stability of V_T and DVR estimates was assessed for each method by progressively truncating the PET data in 10-min increments from the full duration of acquisition down to 50 min. For all graphical methods, the optimal choice for the cutoff time t^* was determined empirically by systematically varying t^* in 5-min increments from 15 to 60 min and assessing linearity of the transformed data as well as stability of resulting V_T or DVR estimates.

Parametric imaging:Dynamic PET images were smoothed with a 3-mm full width at half maximum (FWHM) Gaussian filter and $SUVR_{70–90min}$ as well as $SUVR_{90–120min}$ parametric images were generated.

Statistical analysis

The Akaike information criterion (AIC) was used to assess the relative goodness of fit for alternative compartment models [29]. AIC weights were computed as $AIC_{weight,i} = e^{-0.5\Delta_i} / \sum_k e^{-0.5\Delta_k}$ to demonstrate the probability of one model being favored over the others, where i is the model evaluated, k the total number of models tested in this work, and $\Delta_i = AIC_i - AIC_{min}$, with AIC_{min} the lowest AIC value for the time–activity curve being considered [30].

Quantification methods were compared by linear regressions of DVR measures. The coefficient of determination R^2 and t distribution of the Fisher transformation were used to generate p values for linear regressions. All data are expressed as mean value ± one standard deviation (SD) unless otherwise specified. A p value of 0.05 or less was considered statistically significant.

Results

Participants

Table 1 summarizes the subject demographics. A total of 35 subjects participated in this study. All CTRL subjects ($N = 18$) but three had a CDR global score of 0 and MMSE ≥ 27. Other participants met the National Institute of Aging (NIA) research criteria for MCI with a CDR = 0.5 ($N = 11$) ,or for AD with a global CDR = 1 ($N = 6$). Sixteen subjects (four CTRL, six MCI and six AD) were amyloid-β positive as defined by a FLR DVR > 1.2 [12]. The CTRL and MCI/AD groups were well matched in age (69.0 ± 13.6 vs 67.9 ± 11.6, $p = 0.7959$; two-sample t-test). Eight CTRL, six MCI and two AD subjects had arterial blood sampling.

Arterial input function and blood analysis

Whole blood radioactivity time course was consistent across subjects and studies (Fig. 1a). Whole blood to plasma ratio was 0.66 ± 0.01 after 15 min, and reached a plateau. Percent parent in plasma (%PP) best followed a single exponential

Table 1 Subject demographics

Subject	Status	Sex	Weight (kg)	Age (years)	FLR DVR	MMSE	CDR	Arterial blood data
S1	CTRL	Male	86.3	75	1.08	30	0	yes
S2	CTRL	Female	74.5	73	1.09	30	0	yes
S3	CTRL	Male	63.6	77	1.25	30	0.5	no
S4	CTRL	Male	84.0	76	0.97	30	0.5	yes
S5	CTRL	Female	56.8	45	1.05	30	0	no
S6	CTRL	Female	56.3	75	1.12	28	0	no
S7	CTRL	Female	113.5	78	0.85	30	0	no
S8	AD	Male	70.4	74	1.62	24	1	no
S9	MCI	Male	72.6	56	1.95	26	0.5	yes
S10	MCI	Male	79.5	68	1.07	28	0.5	yes
S11	MCI	Female	58.1	67	1.63	30	0.5	no
S12	MCI	Male	85.4	56	0.96	27	0.5	no
S13	MCI	Female	70.4	63	1.50	26	0.5	yes
S14	AD	Male	74.0	84	1.69	23	1	yes
S15	MCI	Male	70.4	87	1.05	29	0.5	yes
S16	CTRL	Male	84.0	54	1.04	29	0	yes
S17	MCI	Male	72.6	71	1.63	28	0.5	no
S18	MCI	Male	126.7	75	1.31	24	0.5	yes
S19	AD	Male	80.3	58	1.24	13	1	no
S20	AD	Male	102.8	60	1.58	23	1	yes
S21	CTRL	Male	73.2	36	1.06	30	NA	yes
S22	MCI	Male	81.6	82	1.86	27	0.5	yes
S23	AD	Male	93.0	58	1.82	23	1	no
S24	CTRL	Female	81.6	76	1.11	27	0.5	no
S25	CTRL	Male	102.1	72	1.04	27	NA	no
S26	MCI	Male	71.7	83	1.11	27	0.5	no
S27	MCI	Male	109.8	47	1.03	28	0.5	no
S28	CTRL	Male	69.9	55	1.00	29	0	yes
S29	CTRL	Female	60.8	85	1.60	28	0	no
S30	AD	Male	52.6	65	1.66	15	1.0	no
S31	CTRL	Female	101.6	58	0.98	25	0	yes
S32	CTRL	Male	98.4	73	1.02	29	NA	yes
S33	CTRL	Female	68.4	80	0.95	30	0	no
S34	CTRL	Female	106.6	71	1.31	30	NA	no
S35	CTRL	Female	76.7	83	2.08	28	0	no

($T_{1/2}$: 5.43 ± 0.68 min) and revealed rapid metabolism, with 15.3 ± 2.8% of plasma activity attributable to unmetabolized [^{18}F]MK6240 at 15 min and only 6.1 ± 2.3% at 90 min (Fig. 1b). Primarily polar and moderately polar metabolites were observed on HPLC. An example of time course of the different components quantified from the radioHPLC fraction chromatogram is represented in Fig. 1c. On average, no differences in metabolism were found between the CTRL and MCI/AD groups ($p = 0.1819$, two-sample t-test on $T_{1/2}$ values). Figure 1d shows the resulting metabolite corrected arterial input functions. Plasma-free fraction (PFF) was 0.18 ± 0.05 across subjects. No significant differences in PFF was found between CTRL and MCI/AD groups ($p = 0.4251$, two-sample t-test). Since PFF was consistent across subjects and no significant differences was found between groups, PFF was not included in the arterial input function for subsequent analysis.

[^{18}F]MK6240 kinetics in brain

In CTRLs, brain uptake and kinetics were homogenous across brain regions and subjects. [^{18}F]MK6240 peaked quickly in gray matter 2–5 SUV at ~3 min followed by fast washout. MCI subjects demonstrated greater inter-region as well as inter-subject heterogeneity in terms of uptake and kinetics. According to Akaike information criterion (AIC) and visual inspection, for all subjects and brain regions investigated, the preferred compartment model ($AIC_{weight,median} = 1$) was a reversible two-tissue model with vascular contribution (2T4k1v) included as a model parameter (Fig. 2). A reversible two-tissue model with vascular contribution v fixed to $v = 0.05$ (2T4k) provided V_T estimates that were in good agreement with those obtained from the 2T4k1v model ($y = 1.07x - 0.26$, $R^2 = 0.99$, $p < 0.0001$, mean difference: 0.23 ± 0.70 ml.cm^{-3}), except for one subject for which data points of six regions were outside the limit of agreement of the Bland–Altman plot (data not shown). DVR values estimated from these two models were in excellent agreement ($y = 1.02x - 0.02$, $R^2 = 0.99$, $p < 0.0001$, mean difference: 0.003 ± 0.057) for all subjects and brain regions surveyed in this work. Other models tested gave relatively poor model fits and therefore were found to be insufficient. The total volume of distribution (V_T) ranged from 3.9–8.1 ml.cm^{-3} in gray matter and 3.1–5.7 ml.cm^{-3} in white matter for CTRL subjects. MCI/AD

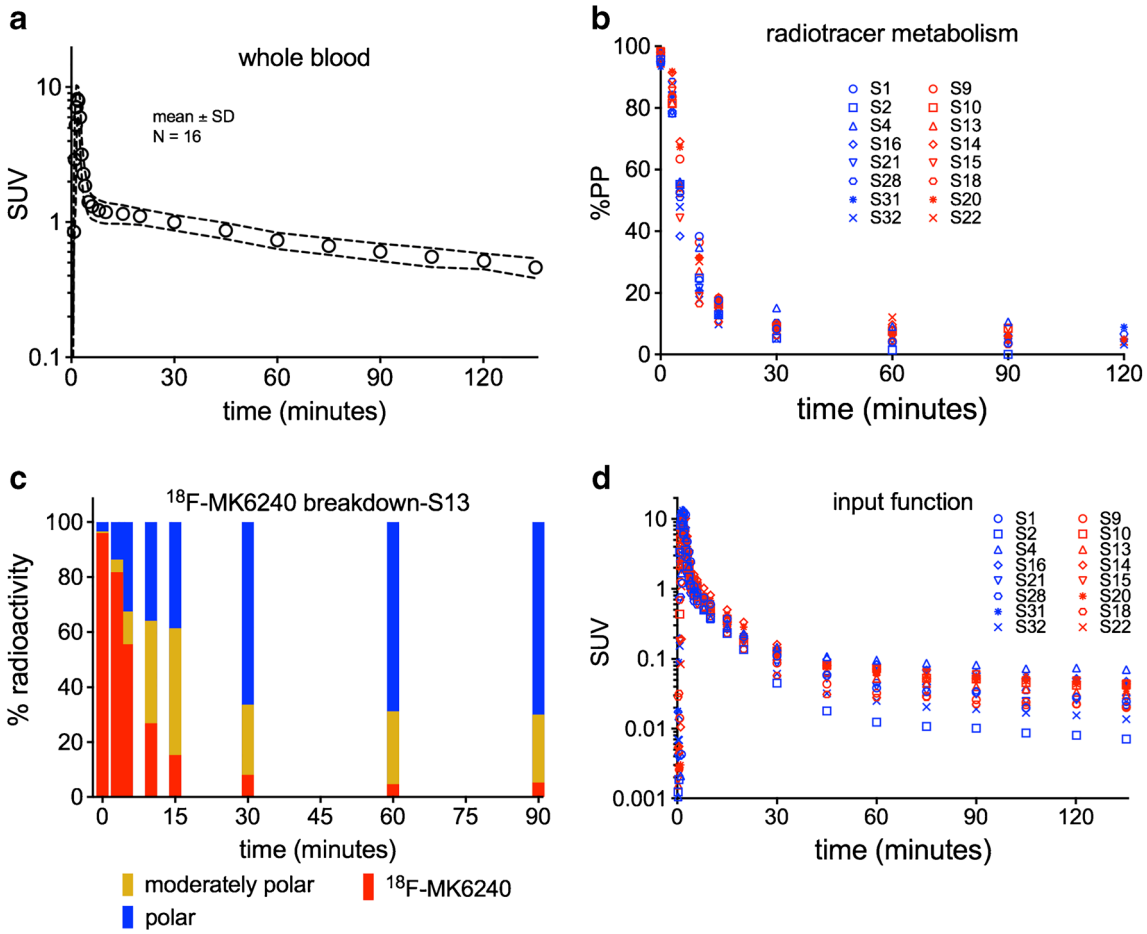

Fig. 1 Arterial blood and plasma data. **a** Mean time course of whole-blood SUV across all subjects with corresponding SD. **b** %Parent in plasma PP of [^{18}F]MK6240 plotted for all subjects. **c** Time course of [^{18}F]MK6240 breakdown in subject S13 with polar, moderately nonpolar, and ^{18}F-MK6240 components depicted in *blue*, *yellow* and *red* respectively. *d* [^{18}F]MK6240 SUV time course in plasma (metabolite-corrected input function)

subjects demonstrated a wide range of V_T, and the highest value was found in the precuneus of an MCI subject (S9) with a V_T of 50.2 ml.cm^{-3}. Table 2 shows the mean of kinetic parameters as well as SD derived from the 2T4k1v model across CTRL and MCI/AD groups. As shown in Supplemental Figure 1, V_T was highly correlated with the volume of distribution of the second compartment (K_1k_3/k_2k_4) ($y = 1.01x + 2.16$, $R^2 = 0.99$, $p < 0.0001$) as well as with k_3/k_4 ($y = 2.28x + 1.96$, $R^2 = 0.87$, $p < 0.0001$). In contrast, the correlation of V_T with the volume of distribution of the first compartment (K_1/k_2) was very weak ($R^2 = 0.05$, $p = 0.001$). No significant differences in cerebellar V_T were found between the CTRL and MCI subject groups (6.8 ± 2.0 ml.cm^{-3} vs 6.3 ± 1.7 ml.cm^{-3}, $p = 0.6027$, unpaired t-test). As shown in Supplemental Figure 2, no significant correlation was found between V_T and K_1 ($R^2 = 0.001$, $p = 0.7133$), and a weak but statistically significant negative correlation was observed between $SUVR_{90\text{-}120min}$ and K_1 ($R^2 = 0.02$, $p = 0.03$).

Simplified methods

Logan plots did not linearize well for all datasets. Nonetheless, using a 40 min t^*, V_T estimated by the Logan graphical method correlated very well with V_T calculated from the micro-parameters obtained from the full compartmental modeling analysis ($y = 0.93x + 0.39$, $R^2 = 0.99$, $p < 0.0001$; mean difference: -0.10 ± 0.63 ml.cm^{-3}; Fig. 3a). The V_T estimates obtained with MA1 (with $t^* = 40$ min) were also highly correlated and in good agreement with those obtained from the reversible two-tissue compartment model ($y = 0.96x + 0.28$, $R^2 = 0.99$, $p < 0.0001$; mean difference: -0.01 ± 0.61 ml.cm^{-3}; Fig. 3b). The Logan graphical method using cerebellar input functions for calculation of DVR linearized very well by t^* of 40 min.

As shown on Fig. 4a and b, Logan DVR and MRTM2, using an estimated average tissue-to-plasma efflux constant $\overline{k'_2}$, were highly correlated with DVR estimates obtained from the 2T4k1v model (2T4k1v DVR), but the slope was less than unity ($y = 0.79x + 0.20$, $R^2 = 0.99$, $p < 0.0001$; Fig. 4a and $y = 0.80x + 0.21$, $R^2 = 0.99$, $p < 0.0001$; Fig. 4b). Consequently, MRTM2 and Logan DVR were in excellent agreement ($y = 1.02x - 0.01$, $R^2 = 0.99$, $p < 0.0001$; Fig. 4c).

DVR estimated from FRTM were linearly correlated with 2T4k1v DVR, but strongly underestimated blood-based DVR ($y = 0.55x + 0.74$, $R^2 = 0.80$, $p < 0.0001$; data not shown). The same observation was made for SRTM ($y = 0.57x + 0.50$, $R^2 = 0.88$, $p < 0.0001$; data not shown).

Finally, $SUVR_{70–90min}$ and $SUVR_{90–120min}$ were also both highly correlated with 2T4k1v DVR, but showed a marked underestimation for DVR > 3 best described by univariate quadratic functions ($R^2 = 0.95$, $p < 0.0001$; Fig. 4d and $R^2 = 0.97$, $p < 0.0001$; Fig. 4g, respectively). For 2T4k1v DVR < 3, both $SUVR_{70–90min}$ and $SUVR_{90–120min}$ show high linear correlations with 2T4k1v DVR with slope close to unity ($y = 0.90x + 0.11$, $R^2 = 0.93$, $p < 0.0001$; Fig. 4d and $y = 0.94x + 0.07$, $R^2 = 0.95$, $p < 0.0001$; Fig. 4g, respectively). SUVRs showed good linear correlations with Logan DVR ($SUVR_{70–90min}$: $y = 0.86x + 0.17$, $R^2 = 0.95$, $p < 0.0001$; Fig. 4e and $SUVR_{90–120min}$: $y = 0.93x + 0.06$, $R^2 = 0.97$, $p < 0.0001$; Fig. 4h), as well as with MRTM2 DVR ($SUVR_{70–90min}$: $y = 0.84x + 0.17$, $R^2 = 0.96$, $p < 0.0001$; Fig. 4f and $SUVR_{90–120min}$: $y = 0.92x + 0.07$, $R^2 = 0.97$, $p < 0.0001$; Fig. 4i) despite a small underestimation of DVR values. Corresponding Bland–Altman plots between the different model outcomes are shown in Supplemental Figure 3.

Time stability of model estimates and SUVR

Figure 5 shows the time stability of V_T and DVR estimates in the temporal cortex of CTRL and MCI/AD subjects.

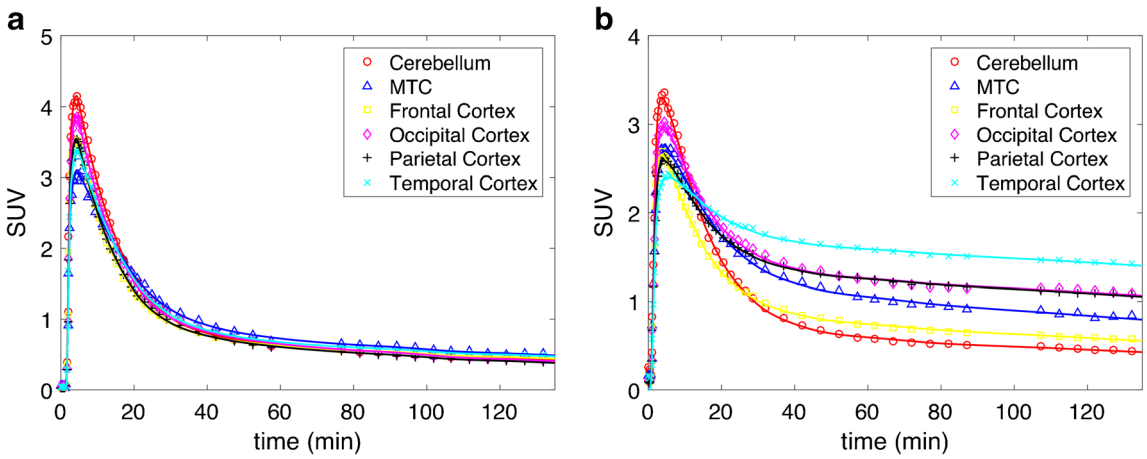

Fig. 2 [^{18}F]MK6240 kinetics in different brain regions (cerebellum, mesial temporal cortex MTC, frontal cortex, occipital cortex, parietal cortex, and temporal cortex). **a** 2T4k1v model fits in a CTRL subject (S1). **b** 2T4k1v model fits in an AD subject (S14). *Markers* represent dynamic PET measurements and *solid lines* depict model fits

Table 2 Mean ± SD of 2T4k1v kinetic parameters obtained for CTRL subjects and MCI/AD group

Subject	Region	K1 (ml/min/cc)	k2 (min^{-1})	k3 (min^{-1})	k4 (min^{-1})	Vascular fraction v	VT (ml/cc)
CTRLs	Cerebellum	0.398 ± 0.082	0.161 ± 0.029	0.015 ± 0.004	0.010 ± 0.004	0.041 ± 0.031	6.8 ± 2.0
	Precuneus	0.409 ± 0.115	0.183 ± 0.042	0.016 ± 0.003	0.010 ± 0.003	0.045 ± 0.035	6.3 ± 1.6
	MTC	0.287 ± 0.065	0.132 ± 0.027	0.016 ± 0.002	0.015 ± 0.006	0.048 ± 0.028	4.8 ± 1.2
	Caudate	0.344 ± 0.120	0.149 ± 0.049	0.014 ± 0.006	0.019 ± 0.008	0.035 ± 0.036	4.1 ± 0.9
	Hippocampus	0.307 ± 0.071	0.136 ± 0.030	0.016 ± 0.003	0.016 ± 0.006	0.050 ± 0.032	4.7 ± 1.0
	Putamen	0.456 ± 0.118	0.149 ± 0.045	0.013 ± 0.003	0.021 ± 0.009	0.045 ± 0.050	5.3 ± 1.6
	Frontal lobe	0.368 ± 0.106	0.183 ± 0.043	0.017 ± 0.002	0.009 ± 0.002	0.048 ± 0.032	5.8 ± 1.2
	Occipital lobe	0.409 ± 0.110	0.179 ± 0.043	0.018 ± 0.003	0.011 ± 0.003	0.038 ± 0.035	6.3 ± 1.8
	Parietal lobe	0.375 ± 0.104	0.176 ± 0.040	0.017 ± 0.003	0.011 ± 0.003	0.042 ± 0.029	5.7 ± 1.4
	Temporal lobe	0.337 ± 0.093	0.150 ± 0.033	0.016 ± 0.002	0.010 ± 0.004	0.041 ± 0.026	6.1 ± 1.7
	White matter	0.193 ± 0.033	0.122 ± 0.023	0.044 ± 0.013	0.029 ± 0.008	0.032 ± 0.018	4.1 ± 1.0
Subject	Region	K1 (ml/min/cc)	k2 (min^{-1})	k3 (min^{-1})	k4 (min^{-1})	Vascular fraction v	VT (ml/cc)
MCIs/ADs	Cerebellum	0.363 ± 0.075	0.161 ± 0.039	0.015 ± 0.004	0.009 ± 0.003	0.036 ± 0.025	6.3 ± 1.7
	Precuneus	0.334 ± 0.061	0.163 ± 0.047	0.030 ± 0.021	0.009 ± 0.004	0.031 ± 0.030	13.2 ± 15.3
	MTC	0.250 ± 0.036	0.127 ± 0.029	0.027 ± 0.008	0.009 ± 0.004	0.050 ± 0.026	9.7 ± 5.5
	Caudate	0.229 ± 0.086	0.129 ± 0.036	0.020 ± 0.005	0.017 ± 0.008	0.028 ± 0.022	3.9 ± 1.2
	Hippocampus	0.268 ± 0.044	0.136 ± 0.023	0.026 ± 0.009	0.011 ± 0.005	0.049 ± 0.026	8.2 ± 5.7
	Putamen	0.414 ± 0.068	0.141 ± 0.041	0.018 ± 0.005	0.018 ± 0.008	0.038 ± 0.029	6.7 ± 2.9
	Frontal lobe	0.295 ± 0.051	0.170 ± 0.040	0.022 ± 0.009	0.008 ± 0.003	0.033 ± 0.023	7.4 ± 4.8
	Occipital lobe	0.325 ± 0.060	0.162 ± 0.039	0.027 ± 0.011	0.008 ± 0.004	0.028 ± 0.025	11.8 ± 9.3
	Parietal lobe	0.281 ± 0.048	0.153 ± 0.045	0.029 ± 0.017	0.008 ± 0.003	0.033 ± 0.024	11.8 ± 12.1
	Temporal lobe	0.262 ± 0.050	0.132 ± 0.035	0.031 ± 0.014	0.007 ± 0.003	0.033 ± 0.021	13.8 ± 10.1
	White matter	0.190 ± 0.020	0.126 ± 0.041	0.042 ± 0.010	0.022 ± 0.007	0.030 ± 0.016	5.2 ± 2.6

Blood-based methods (2T4k1v, Logan, and MA1 graphical methods) showed an increasing underestimation of V_T estimates as the scan duration was being truncated down to 50 min. This underestimation was greater in high-binding regions of MCI/AD subjects than in CTRLs. Furthermore, Logan and MA1 graphical methods were more affected than the 2T4k1v model (Fig. 5a–c), consistent with the relatively poor level of linearization observed. In contrast, DVR estimates of reference-based graphical methods were more stable with time (Fig. 5d–e). Lastly, SUVR was still increasing at 135 min post injection in very high binding regions of MCI/AD subjects, while it was stable by 30 min in CTRL subjects (Fig. 5f).

Parametric imaging

Figure 6 shows $SUVR_{70–90min}$ and $SUVR_{90–120min}$ maps for all subjects studied in this work, as well the corresponding

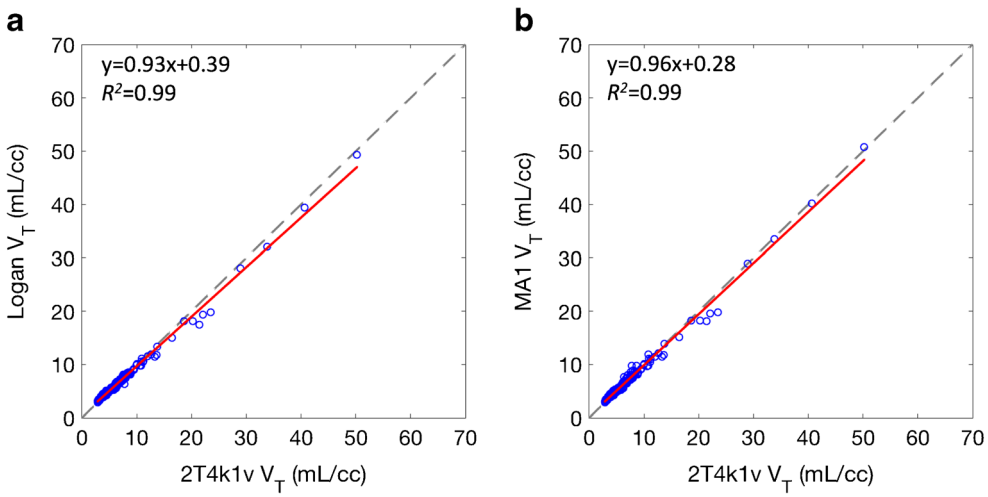

Fig. 3 Comparisons between blood-based analysis methods. **a** Correlation plots of Logan V_T against V_T calculated from the 2T4k1v model. **b** Correlation plots of MA1 V_T against V_T calculated from the 2T4k1v model. *Red lines* represent linear regression and *gray dashed lines* are lines of identity

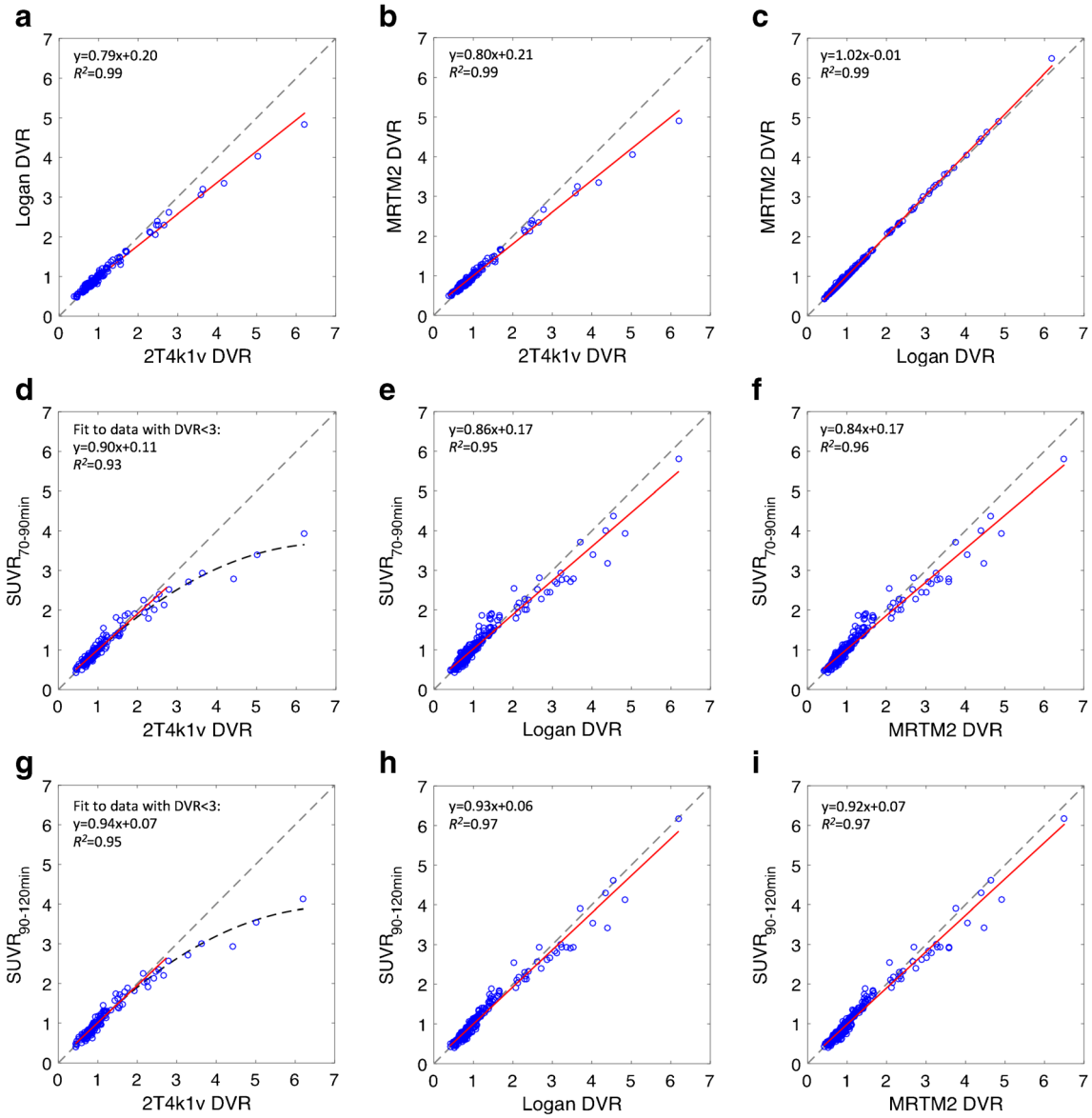

Fig. 4 **a**–**i**) Correlation plots showing the relationship between the outcomes of different quantification methods surveyed in this work: 2T4k1v DVR, Logan DVR (with cerebellar input functions), MRTM2 DVR, $SUVR_{70\text{-}90min}$ and $SUVR_{90\text{-}120min}$. *Red lines* represent linear regression and *gray dashed lines* are lines of identity. *Black dashed lines* in **d**, **g** represent fits obtained with univariate quadratic functions, and are meant to highlight the roll-off effect observed for 2T4k1v DVR > 3. Data points presented on these plots are from all subjects and brain regions surveyed in this work

MRI slices for anatomical reference. All MCI/AD subjects presenting elevated [^{18}F]MK6240 binding were also amyloid-β positive. Moreover, none of the CTRL subjects exhibited [^{18}F]MK6240 uptake consistent with neurofibrillary tau deposition patterns established in the literature. For the most part, off-target binding was concordant with what was previously reported in Betthauser et al. [9]. In particular, all subjects demonstrated significant binding in the ethmoid sinus as well as in the retina (probably binding to melanin). All CTRL subjects, as well as most of the MCI/AD subjects, exhibited various degrees of uptake in the meninges.

Discussion

[^{18}F]MK6240 was developed for in-vivo quantification of NFT, and despite rapid adoption in human imaging studies there have to date been only limited reports on characterization of pharmacokinetics and data analysis strategies. In this work, we extended previous works to provide a comparison of the different pharmacokinetic modeling strategies ranging from the more complex fully quantitative methods using arterial blood sampling to the simpler SUVR analysis.

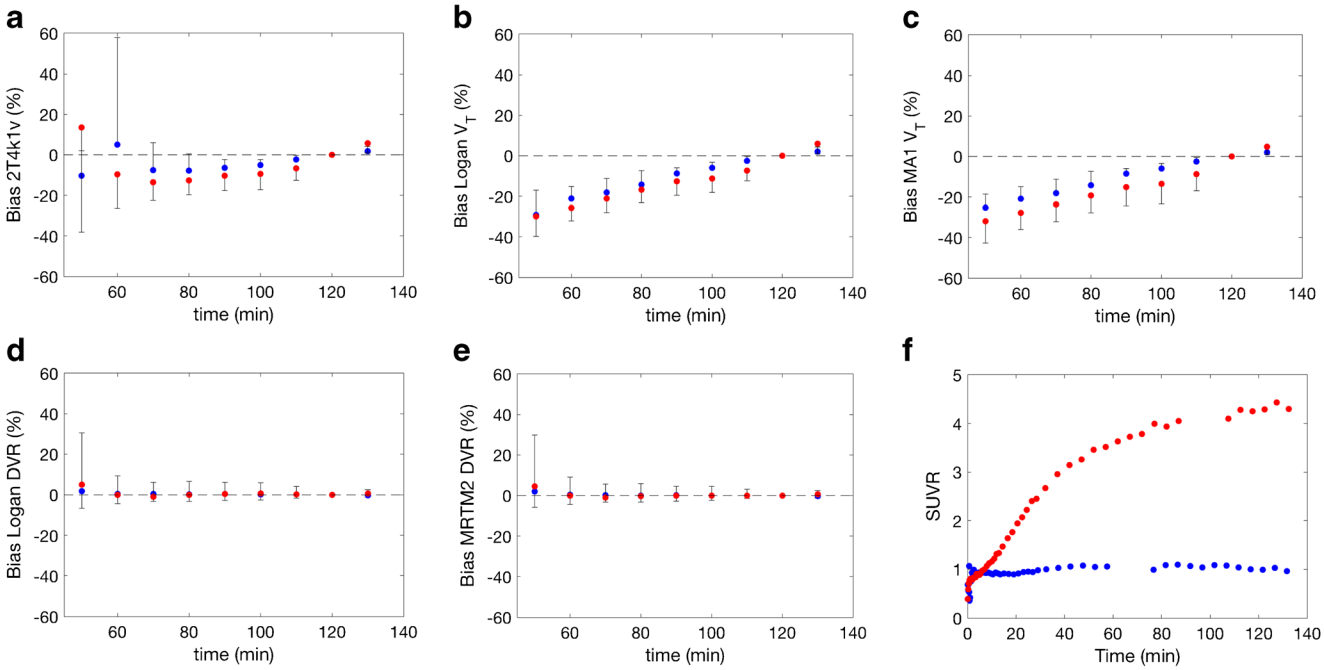

Fig. 5 **a**–**e** Time stability of V_T and DVR estimates in the temporal cortex for the different methods surveyed in this work with truncated acquisition times down to 50 min post tracer injection. For each method, bias was calculated by taking the 120 min acquisition as the reference. **f** SUVR time course in the precuneus measured for a representative CTRL subject (*S1*) and for an MCI subject showing high [^{18}F]MK6240 uptake (*S9*). *Blue markers* are for control subjects and *red markers* are for MCI/AD subjects. **a**–**e** show mean and SD calculated across subjects

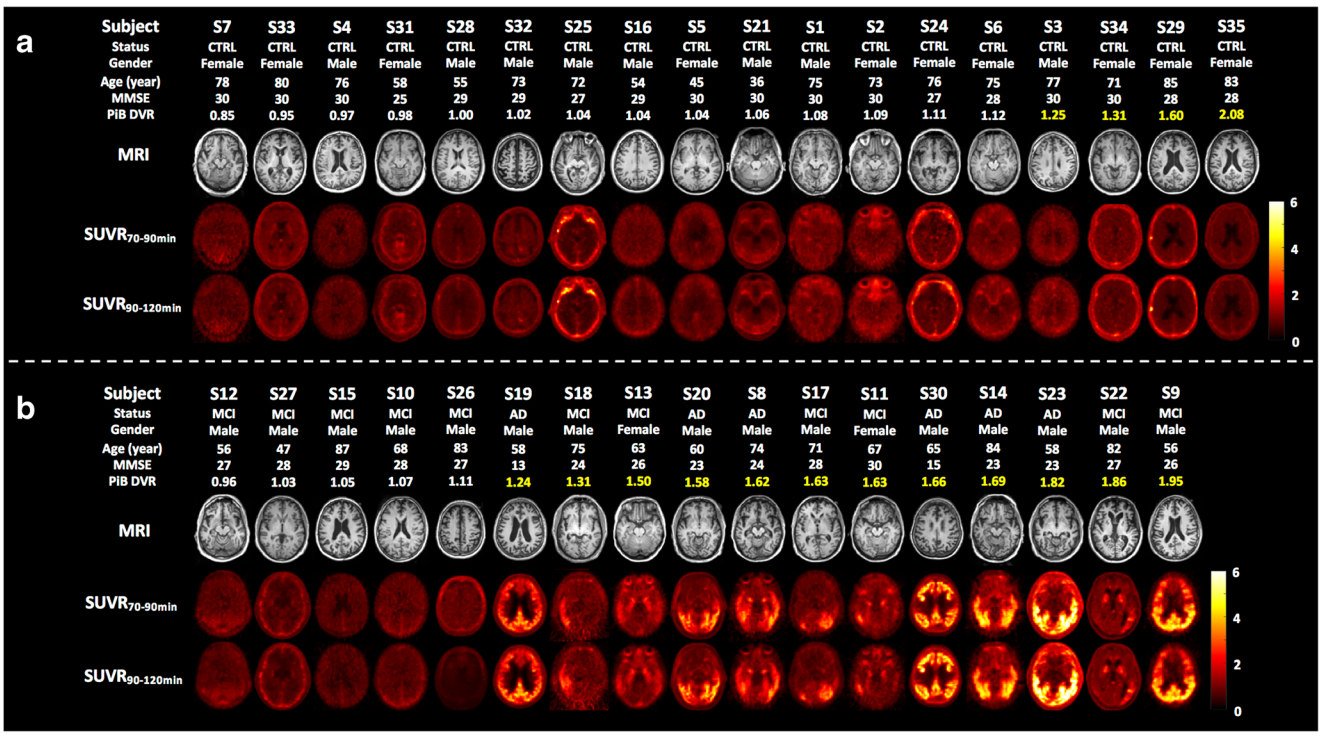

Fig. 6 SUVR parametric images of [^{18}F]MK6240 for all subjects using the cerebellum as reference region. All images were registered into the MNI template space. Panel **a** shows CTRL subjects and panel **b** shows MCI/AD subjects. Within each group, subjects were sorted by PiB scores when applicable. Amyloid-β positive scores are highlighted in *yellow*. In each panel, *first row* shows the corresponding individual MPRAGE images for anatomical reference

Quantification using arterial blood data

[^{18}F]MK6240 kinetics was best described with a reversible two-tissue compartment model, with vascular contribution included as a model parameter (2T4k1v), for all subjects and for both low and high binding regions. Our findings suggest that elevated V_T estimates were mostly driven by specific binding (Supplemental Figure 1). We did not find any significant correlation between V_T and K_1, and observed a weak but significant negative correlation between $SUVR_{90–120min}$ and K_1, suggesting that these outcomes are not dependent on potential perfusion changes. Also, cerebellar V_T estimates were not significantly different between CTRL and MCI subjects, further supporting the use of the cerebellum as a reference region (i.e., devoid of specific binding) for non-invasive quantification methods. Therefore, in this work, cerebellar V_T was used as an index of non-displaceable binding. Despite a relatively poor linearization of the Logan graphical method in most datasets, we observed a very good agreement in V_T estimates between the arterial blood-based graphical methods (Logan and MA1) and the preferred 2T4k1v model when using a 40-min t^*.

Reference region methods and SUVR

We examined simplified methods for quantification of [^{18}F]MK6240 uptake, using the cerebellum as a reference region. DVR from FRTM and SRTM linearly correlated with blood-based DVR estimates, but demonstrated a significant underestimation and therefore were not further investigated. The reason of this underestimation, seen despite relatively good model fits in high binding regions, can be explained by violation(s) of at least one of the model assumptions [31]. In particular, one of the model assumptions that was violated is the description of the kinetic behavior of the tracer by a 1 T model in the reference region for FRTM and in the reference and target tissues for SRTM. Indeed, for all brain regions the time–activity curves (including those for the reference region used in this work) were best fitted by a two-tissue model, and a simple one-tissue model clearly failed to fit the data. As specified in the methods, for both Logan DVR and MRTM2 we used an estimated average tissue-to-plasma efflux constant $\overline{k'_2}$ fixed to the average of k'_2 cerebellar values calculated from the 2T4k1v microparameters across subjects scanned with arterial blood sampling. These reference region-based graphical methods (Logan and MRTM2) and late SUVRs were highly correlated with DVR estimates obtained from compartmental modeling and arterial sampling (DVR_{2T4k1v}), but underestimated DVR_{2T4k1v} at DVR > 3. Underestimation of 2T4k1v DVR by the graphical methods was due to the error term $\delta = DVR\left(\frac{1}{k'_2}-\frac{1}{\overline{k'_2}}\right)\frac{REF(t)}{ROI(t)}$ [24, 26], since using individual k'_2 cerebellar estimates to perform a similar comparison as in Fig. 4a provided better agreement (y = 0.92 + 0.08, $R^2 = 0.99$, $p < 0.0001$; mean difference: -0.002 ± 0.078 ml.cm^{-3}; data not shown). In very high binding regions ($DVR_{2T4k1v} > 3$), SUVR was still increasing at 135 min and therefore did not reach equilibrium throughout the scan duration (Fig. 5f), which certainly contributed to the SUVR underestimation when compared to DVR_{2T4k1v}. This effect is probably due to the slow kinetics of [^{18}F]MK6240 in an NFT-rich region because of its subnanomolar affinity for NFTs. These underestimations at high DVR were also observed, although to a lesser extent, by Pascoal et al. in a subset of six subjects [11]. It was not clear however, how many subjects presented DVR values greater than 3 in their study. In contrast, Lolith et al. also presented good correlations between reference region-based methods and DVR_{2T4k1v} using 90 min of PET data, but reported different slopes across subjects. However, all their MCI/AD subjects ($N = 3$) exhibited $DVR_{2T4k1v} < 2.5$. Lastly, part of the discrepancies observed between reference region-based methods and blood-based methods may be explained by potential measurement errors due to the fast metabolism of [^{18}F]MK6240 as discussed below.

[^{18}F]MK6240 metabolism

[^{18}F]MK6240 was metabolized quickly and, consequently, %PP was very low after 30 min post tracer injection (typically < 10% of the radioactivity concentration measured in the plasma), which is consistent with the data reported by both Lolith et al. and Pascoal et al. [10, 11]. Although arterial blood-based compartmental modeling is commonly considered as the gold standard, this fast metabolism is a potential concern for the accuracy of in-vivo quantification of NFT with [^{18}F]MK6240 using arterial blood-based methods. Indeed, at late time points small errors in low PP can potentially introduce substantial bias in the kinetic parameters k_3-k_4 and therefore in V_T, particularly in high-binding regions.

Limitations

One limitation of this work includes the absence of test–retest data to assess the intra-subject reproduciblity of our quantitative measurements, which would be particularly useful in determining the accuracy with which we will be able to assess small changes in tau deposition at early stages of the disease, in response to therapy or for statistical or longitudinal analyses. However, we found relatively low variability in V_T estimates measured accross CTRL subjects compared to the wide range of V_T values measured in the MCI/AD group. These results suggest that test–retest variability would probably be low, at least in CTRLs, in view of the wide dynamic range of [^{18}F]MK6240 signal measured across MCI and AD subjects. Nonetheless, in regard to the fast metabolism of [^{18}F]MK6240 discussed above, test–retest studies would be particularly informative in MCI/AD subjects presenting brain regions with

high density of NFT. These studies would also be very valuable to assess the reproducibility of Logan DVR and MRTM2 using a fixed $\overline{k'_2}$ value. Another limitation of the present study was the limited number of MCI/AD subjects with arterial blood sampling presenting very high DVR (DVR > 3) (N = 2), i.e., where we observed some discrepancies between the outcomes of the different quantification methods.

In conclusion, [^{18}F]MK6240 seems to exhibit exquisite affinity for NFT and consequently demonstrated a wide dynamic range of uptake in MCI/AD subjects as compared to CTRLs. However, measurement of parent in plasma showed fast metabolism with little radioactivity in the parent form after 60 min, which is a potential concern for accurate quantification of tau aggregates using blood-based methods. For all subjects, the preferred compartmental model was a reversible two-tissue model with the vascular contribution included as a model parameter (2T4k1v). Despite not being very stable in time, the blood-based Logan and MA1 graphical methods resulted in good agreement with 2T4k1v for the estimation of V_T when using a 40-min t^* and the full duration of the PET measurements. Reference region-based methods correlated strongly with the full compartment analysis, but underestimated DVR_{2T4k1v} at DVR > 3. Therefore, caution should be applied when using simplified methods to such data sets and in quantitative interpretation of corresponding outcomes. Moreover, in very high binding regions/subjects, SUVR was still increasing at 135 min, making this simplified method sensitive to uptake time variation. In light of this observation, studies using late SUVR as a quantitative outcome will require adhering strictly to a static imaging time window.

Acknowledgements This work was supported by the following grants: R01AG046396, S10OD018035, P41EB022544, and T32 EB005876. The authors thank Julia Scotton and Nicole DaSilva for subject preparation, scanning, and monitoring, as well as Steven Weise and Eugene Lee for their help with data management.

Funding This study was funded by R01AG046396, S10OD018035, T32 EB005876, and P41EB022544.

Compliance with ethical standards

Conflict of interest Nicolas J. Guehl declares that he has no conflict of interest. Dustin W. Wooten declares that he has no conflict of interest. Daniel L. Yokell declares that he has no conflict of interest. Sung-Hyun Moon declares that he has no conflict of interest. Maeva Dhaynaut declares that she has no conflict of interest. Samantha Katz declares that she has no conflict of interest. Kirsten A. Moody declares that she has no conflict of interest. Codi Gharagouzloo declares that he has no conflict of interest. Aurélie Kas declares that she has no conflict of interest. Keith A. Johnson declares that he has no conflict of interest. Georges El Fakhri declares that he has no conflict of interest. Marc D. Normandin declares that he has no conflict of interest.

Ethical approval All procedures performed in studies involving human participants were in accordance with the ethical standards of the institutional and/or national research committee and with the 1964 Helsinki Declaration and its later amendments or comparable ethical standards.

Informed consent Informed consent was obtained from all individual participants included in the study

References

1. Braak H, Braak E. Neuropathological stageing of Alzheimer-related changes. Acta Neuropathol. 1991;82:239–59.
2. Arriagada PV, Growdon JH, Hedley-Whyte ET, Hyman BT. Neurofibrillary tangles but not senile plaques parallel duration and severity of Alzheimer's disease. Neurology. 1992;42:631–9.
3. Villemagne VL, Fodero-Tavoletti MT, Masters CL, Rowe CC. Tau imaging early progress and future directions. Lancet Neurol. 2015;14:114–24.
4. Okamura N, Harada R, Ishiki A, Kikuchi A, Nakamura T, Kudo Y. The development and validation of tau PET tracers: current status and future directions. Clin Transl Imaging. 2018;6:305–16.
5. Leuzy A, Chiotis K, Gilberg PG, Almkvist O, Rodriguez-Vieitez E, Nordberg A. Tau PET imaging in neurodegenerative taupathies-still a challenge. Mol Psychiatry. 2019. https://doi.org/10.1038/s41380-018-0342-8.
6. Hall B, Mak E, Cervenka S, Aigbirhio FI, Rowe JB, O'Brien JT. In vivo tau PET imaging in dementia: pathophysiology, radiotracer quantification, and a systematic review of clinical findings. Ageing Res Rev. 2017;36:50–63.
7. Walji AM, Hostetler ED, Selnick H, Zeng Z, Miller P, Bennacef I, et al. Discovery of 6-(Fluoro-(18)F)-3-(1H-pyrrolo[2,3-c]pyridin-1-yl)isoquinolin-5-amine ([(18)F]-MK-6240): a positron emission tomography (PET) imaging agent for quantification of neurofibrillary tangles (NFTs). J Med Chem. 2016;59:4778–89.
8. Hostetler ED, Walji AM, Zeng Z, Miller P, Bennacef I, Salinas C, et al. Preclinical characterization of 18F-MK-6240, a promising PET tracer for in vivo quantification of human neurofibrillary tangles. J Nucl Med. 2016;57:1599–606.
9. Betthauser TJ, Cody KA, Zammit MD, Murali D, Converse AK, Barnhart TE, et al. In vivo characterization and quantification of neurofibrillary tau PET radioligand [^{18}F]MK-6240 in humans from Alzheimer's disease dementia to young controls. J Nucl Med. 2019;60(1):93–9. https://doi.org/10.2967/jnumed.118.209650.
10. Lohith TG, Bennacef I, Vandenberghe R, Vandenbulcke M, Salinas-Valenzuela C, Declercq R, et al. J Nucl Med. 2018;60(1):107–14. https://doi.org/10.2967/jnumed.118.208215.
11. Pascoal TA, Shin M, Kang MS, Chamoun M, Chartrand D, Mathotaarachchi S, et al. In vivo quantification of neurofibrillary tangles with [^{18}F]MK-6240. Alzheimers Res Ther. 2018;10:74.
12. Johnson KA, Schultz A, Betensky RA, Becker JA, Sepulcre J, Rentz D, et al. Tau PET imaging in aging and early Alzheimer's disease. Ann Neurol. 2016;79:110–9.
13. Collier TL, Yokell DL, Livni E, Rice PA, Celen S, Serdons K, et al. cGMP production of the radiopharmaceutical [^{18}F]MK-6240 for PET imaging of human neurofibrillary tangles. J Label Compd Radiopharm. 2017;60:263–9.
14. Adam LE, Zaers J, Ostertag H, Trojan H, Bellemann ME, Brix G. Performance evaluation of the whole-body PET scanner ECAT EXACT HR+ following the IEC standard. IEEE Trans Nucl Sci. 1997;44:1172–9.
15. Karakatsanis N, Sakellios N, Tsantilas NX, et al. Comparative evaluation of two commercial PET scanners, ECAT EXACT HR+ and

biograph 2, using GATE. Nucl Instrum Methods Phys Res Sect A Accel Spectrom Detect Assoc Equip. 2006;569:368–72.
16. Collier T, Normandin MD, El Fakhri G, Vasdev N. Automation of column-switching HPLC for analysis of radiopharmaceuticals and their metabolites in plasma. Soc Nucl Med Ann Meet Abstr. 2013;54:1133.
17. Hilton J, Yokoi F, Dannals RF, Ravert HT, Szabo Z, Wong DF. Column-switching HPLC for the analysis of plasma in PET imaging studies. Nucl Med Biol. 2000;27:627–30.
18. Wooten DW, Guehl NJ, Verwer EE, Shoup TM, Yokell DL, Zubcevik N, et al. Pharmacokinetic evaluation of the tau PET radiotracer ^{18}F-T807 (^{18}F-AV-1451) in human subjects. J Nucl Med. 2017;58:484–91.
19. Alpert NM, Berdichevsky D, Levin Z, Morris ED, Fischman AJ. Improved methods for image registration. Neuroimage. 1996;3:10–8.
20. Jenkinson M, Beckman CF, Behrens TEJ, Woolrich MW, Smith SMFSL. NeuroImage. 2012;62:782–90.
21. Innis RB, Cunningham VJ, Delforge J, Fujita M, Gjedde A, Gunn RN, et al. Consensus nomenclature for in vivo imaging of reversibly binding radioligands. J Cereb Blood Flow Metab. 2007;27:1533–9.
22. Logan J, Fowler JS, Volkow ND, Wolf AP, Dewey SL, Schlyer DJ, et al. Graphical analysis of reversible radioligand binding from time-activity measurements applied to [N-11C-methyl]-(−)-cocaine PET studies in human subjects. J Cereb Blood Flow Metab. 1990;10:740–7.
23. Ichise M, Toyama H, Innis RB, Carson RE. Strategies to improve neuroreceptor parameter estimation by linear regression analysis. J Cereb Blood Flow Metab. 2002;22:1271–81.
24. Logan J, Fowler JS, Volkow ND, Wang GJ, Ding YS, Alexoff DL. Distribution volumes ratios without blood sampling from graphical analysis of PET data. J Cereb Blood Flow Metab. 1996;16:834–40.
25. Ichise M, Liow JS, Lu JQ, Takano A, Model K, Toyama H, et al. Linearized reference tissue parametric imaging methods: application to [11C]DASB positron emission tomography studies of the serotonin transporter in human brain. J Cereb Blood Flow Metab. 2003;23:1096–112.
26. Logan J. A review of graphical methods for tracer studies and strategies to reduce bias. Nucl Med Biol. 2003;30:833–44.
27. Cunningham VJ, Hume SP, Price GR, Ahier RG, Cremer JE, Jones AK. Compartmental analysis of diprenorphine binding to opiate receptors in the rat in vivo and its comparison with equilibrium data in vitro. J Cereb Blood Flow Metab. 1991;11:1–9.
28. Lammertsma AA, Hume SP. Simplified reference tissue model for PET receptor studies. Neuroimage. 1996;4:153–8.
29. Akaike H. A new look at the statictical model identification. IEEE Trans Autom Control. 1974;19:716–23.
30. Burnham KP, Andersen DR. Model selection and multimodel inference: a practical information-theoretic approach. 2nd ed. New York: Springer; 2002.
31. Salinas CA, Searle GE, Gunn RN. The simplified reference tissue model: model assumption violations and their impact on binding potential. J Cereb Blood Flow Metab. 2015;35:304–11.